Journal of Non-Newtonian Fluid Mechanics 234 (2016) 201–214

Contents lists available at ScienceDirect

Journal of Non-Newtonian Fluid Mechanics

journal homepage: www.elsevier.com/locate/jnnfm

Steady viscoelastic film flow over 2D Topography: II. The effect of capillarity, inertia and substrate geometry

M. Pavlidis, G. Karapetsas, Y. Dimakopoulos, J. Tsamopoulos*

Laboratory of Computational Fluid Dynamics, Department of Chemical Engineering, University of Patras, Patras 26500, Greece

ARTICLE INFO

Article history:
Received 22 March 2016
Revised 18 June 2016
Accepted 20 June 2016
Available online 1 July 2016

Keywords:
Viscoelastic film flow
Flow over topography
Ptt fluid model
Film flow with inertia

ABSTRACT

We examine the two-dimensional, steady flow of a viscoelastic film under the action of gravity over a substrate with periodic topographical features. We account for the rheology of the viscoelastic material using the exponential Phan–Thien and Tanner (PTT) constitutive model. The conservation equations are solved via the mixed finite element method combined with a quasi-elliptic grid generation scheme, while the viscoelastic stresses are discretized using the EVSS-G/SUPG method. Our scheme allows the computation of accurate steady-state solutions up to high values of Deborah, Reynolds and capillary numbers. We perform a thorough parametric analysis to investigate the effect of the elastic, capillary and inertia forces on the flow characteristics. Our results indicate that surface tension and elasticity affect the film closer to the location with abrupt changes of the substrate topography; the sizes of the capillary ridge before a step down and of the depression before a step up are increased and move upstream as fluid elasticity or interfacial tension increase. It is shown that under creeping flow conditions the length scale of the capillary ridge increases with *De* following a power law of ¼, which can also be predicted by simple scaling arguments. Inertia has a more global effect on the film affecting larger portions of it, while in its presence the length scale of the capillary features is not affected significantly by the material elasticity. Moreover, it is shown that similarly to the case of Newtonian liquids, high inertia causes the formation of a ridge just after the step up. We also explore the effect of the geometrical characteristics of the substrate as well as its inclination angle and it is shown that the interface shape becomes more deformed as the topography appears wider, deeper or it approaches the vertical plane.

1. Introduction

The flow of liquid films over a solid substrate with variable topography is encountered in various liquid-film deposition and printing processes, in arrangements aiming at intensifying heat or mass transfer operations or, on a much larger scale, in various geological phenomena. Typical examples include spin coating (Stillwagon and Larson [1]), gravure printing (Booth [2], Yin and Kumar [3] and Schwartz et al. [4]), flows in two-phase heat exchangers and in adsorption or distillation columns using structured packings (Argyriadi et al. [5]), mudslides and lava flows (Balmforth et al. [6]). In these applications, the flow is typically driven by a body force (such as gravity or centrifugal force) or can be driven by the motion of the substrate itself. The topography may have the form of periodic or localized depressions, protrusions, corrugations or arrested particles and bubbles on the substrate. Naturally, the presence of these topographic variations can lead to undesirable thickness variations of the coated layer or, conversely, can be exploited, for example, to intensify the desired mixing of the material in the film through induced fluid recirculation. Often, the flowing material is a polymeric solution or a suspension of particles which exhibit non-Newtonian properties (e.g. viscoelastic properties). The presence of viscoelasticity may considerably affect the flow, introducing interesting effects on the flow arrangement and the film shape. This will be the subject of the present work. Our goal is to thoroughly investigate the effect of the elastic, capillary and inertia forces on the flow characteristics of a viscoelastic liquid flowing over a substrate with periodic topographical features of different sizes.

Not surprisingly, film flows over topography have received considerable attention in the literature (informative reviews can be found in Pavlidis et al. [7] and Cao et al. [8]). Experimental investigations include the work of Argyriadi et al. [5] who studied the wave formation along the periodic corrugations of the inclined plane and the effect of corrugation steepness and fluid inertia on the static shapes of the film. They also reported conditions under which the flow is stabilized or evolves from 2D steady flow into traveling waves or to near-solitary humps or to 3D flow consisting

* Corresponding author.
E-mail address: tsamo@chemeng.upatras.gr (J. Tsamopoulos).

http://dx.doi.org/10.1016/j.jnnfm.2016.06.011
0377-0257/

of transverse arrays of depressions along the corrugation valleys. Decré and Baret [9] quantified images of the film surface flowing over step, trench, rectangular or square topographies of various depths and lateral dimensions and film thicknesses up to 120 μm and compared them with theoretical predictions. In addition, Wierschem & Aksel [10] and Scholle et al. [11] examined the effect of film inertia and thickness on the separation eddies created in the valleys of a corrugated wall.

An early attempt to address this problem theoretically was made by Pozrikidis [12] who studied the 2D flow over a wavy wall using the boundary integral method under the Stokes flow assumption. The same method was later used by Mazouchi and Homsy [13] for the study of the 2D flow inside and out of a square trench and by Blyth and Pozrikidis [14] for examining the flow over a 3D obstacle attached on the substrate. Alternatively and more frequently, the lubrication (long-wave) approximation has been employed in such studies using topography-adjusted lubrication models, which, under conditions (low values of Ca), were able to retain relatively sharp and nearly rectangular the indentations of the wall. In this context, Stillwagon and Larson [1] were the first who used it to determine the film thickness variation over a trench as it arises in spin coating. Kalliadasis et al. [15] determined the effect of the geometry of the trench or mount on the film characteristics, while Tseluiko et al. [16] examined the possibility of eliminating the film thickness variations by applying an electric field normal to the substrate. Lenz and Kumar [17], on the other hand, investigated the case where there are two layers confined in a channel, with one of the walls having topographical features. The stability of Newtonian film flow over a step-down has been reported by Kaliadasis and Homsy [18] for linear 2D disturbances and by Bielarz and Kalliadasis [19] to nonlinear 2D and 3D disturbances. It has been shown that under the long-wave assumption the film is stable, although the flow could be unstable based on the similarity of the capillary ridge formed here before the step down to that formed in a drop spreading on a rotating substrate, which leads to the formation of rivulets, Fraysse and Homsy [20].

The limitations of the former approaches were investigated by Gaskell et al. [21] and Veremieiev et al. [22] by actually solving the exact NS equations in the presence of 2D square trenches. Similarly, Zhou and Kumar [23] examined the limitations of lubrication theory for two-layer flow in a channel containing a step. Heining et al. [24], on the other hand, examined the emergence of higher harmonics on a film surface flowing over a wavy wall and compared these results with those obtained via the integral boundary-layer approximation. Extensive numerical solutions of the Navier-Stokes equations for steady film flow over 2D periodic topographies with finite inertia and capillarity have also been reported by Malamataris and Bontozoglou [25] and Bontozoglou and Serifi [26] using the finite element method. In the latter study, interesting order-of-magnitude arguments of the gravity, capillary and inertia terms in the momentum balance demonstrated that the computed streamwise length of the capillary ridge/depression decreases with Re, while its dependence on capillarity changes from $Ca^{-1/3}$ to $Ca^{-1/2}$ as inertia increases from zero. Moreover, the height of the capillary features first grows but then decreases with increasing inertia, when finally the latter dominates capillarity.

Despite the fact that polymeric solutions are typically used in spin coating, the effect of viscoelasticity has been largely ignored in the literature. In the first part of our study (Pavlidis et al. [7]) we examined the viscoelastic flow, using the exponential Phan-Tien and Tanner (ePTT) model, over a 2D trench under creeping flow conditions. These conditions are relevant in spin coating where, primarily, the very small film thickness $\tilde{H}_o = O(1\ \mu\text{m})$ restrains the Reynolds number to values well below unity. However, in other processes the film thickness and its velocity may increase considerably, as for example in the case of gravure printing, where thicker films arise ($\tilde{H}_o = O(100\ \mu\text{m})$) over patterns of similar depth and width flowing at much higher speeds than in spin coating ($\tilde{U} \approx 10m/s$), hence increasing the Reynolds number up to 10. Moreover, in heat and mass transfer operations the film Reynolds number can increase up to $O(200)$. The interaction of fluid inertia and elasticity has been studied by Saprykin et al. [27] albeit under the long-wave approximation and assuming that $De \ll 1$; The Deborah number is typically defined as the ratio of the fluid relaxation time and the characteristic time of the flow, and it is often used as a measure of the elastic properties of the viscoelastic liquid. Therefore it is important to extend our previous study in order to thoroughly examine the interplay of inertia forces with capillary, viscous and elastic forces and their effect on the film thickness and planarization efficiency over steep topographical changes of the substrate. To this end, we will not rely on the lubrication approximation, because it inadvertently underestimates the normal elastic stresses (e.g. see [28–31]). In addition, we will employ a constitutive model that allows for more realistic variation of the shear and extensional fluid viscosities with the local rate of strain components, such as the ePTT model [32,33]. In this way we will eliminate the main assumptions used by Saprykin et al. [27] and study more general geometries and fluids with larger elastic effects, i.e. of the same or larger magnitude than the viscous stresses (not perturbations of known results for Newtonian fluids).

The rest of this paper is organized as follows: In Section 2, we briefly present the problem formulation and the solution method used, since the interested reader may find more details in our previous paper (Pavlidis et al. [7]). In Section 3, we validate our numerical code by comparing its predictions with finite inertia to those reported previously for Newtonian fluids. In Section 4, we present scaling laws as well as numerical results for the effect of elasticity, capillarity and inertia and the influence of geometry on substrate planarization. Finally concluding remarks are drawn in Section 5.

2. Problem formulation and method of solution

We consider the steady, two-dimensional film-flow of a viscoelastic fluid driven by a body force over a substrate with isolated or periodic square-trenches. In what follows, the tilde indicates that the quantity under it has dimensions. The fluid is considered to be incompressible with constant density $\tilde{\rho}$, surface tension $\tilde{\sigma}$, relaxation time $\tilde{\lambda}$ and total dynamic viscosity under zero shear $\tilde{\mu} = \tilde{\mu}_s + \tilde{\mu}_p$; $\tilde{\mu}_s$ and $\tilde{\mu}_p$ are the viscosities of the solvent and the polymer, respectively. The viscoelastic film thickness at the entrance of the flow domain is denoted with $\tilde{H}_o$; a schematic of the flow geometry is presented in Fig. 1. At a distance $\tilde{L}_1$ from the entrance, the film encounters an orthogonal trench with length $\tilde{L}_2$, while the distance from the right end of the trench to the exit of the flow domain is denoted with $\tilde{L}_3$. $\tilde{D}$ denotes the position of the bottom wall of the trench. The flow is considered as gravity-driven (although the analysis for centrifugally-driven flow in spin coating is similar as explained in Pavlidis et al. [7]), with α the inclination angle that the substrate forms with the horizontal direction and $\tilde{g}$ the magnitude of the gravitational acceleration. Under the action of gravity, a steady flow is generated.

We scale all lengths with the film thickness, $\tilde{H}_o$, and velocities with the cross-sectional average film velocity, $\tilde{U}$, at the entrance, while the pressure and stress components are scaled with a viscous scale, $\tilde{\mu}\tilde{U}/\tilde{H}_o$. The dimensionless groups that arise are the Reynolds number, $Re = \tilde{\rho}\tilde{U}\tilde{H}_o/\tilde{\mu}$, the capillary number, $Ca = \tilde{\mu}\tilde{U}/\tilde{\sigma}$, the Deborah number, $De = \tilde{\lambda}\tilde{U}/\tilde{H}_o$, the generalized Stokes number, $St = \tilde{\rho}\tilde{g}\tilde{H}_0^2/(\tilde{\mu}\tilde{U})$, the ratio of the solvent viscosity over the total viscosity, $\beta = \tilde{\mu}_s/\tilde{\mu}$, and the geometric ratios $l_1 = \tilde{L}_1/\tilde{H}_o$, $l_2 = \tilde{L}_2/\tilde{H}_o$,

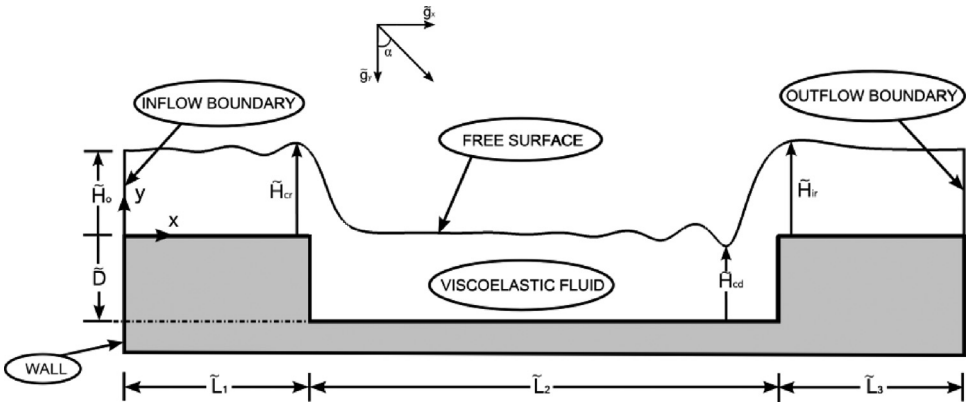

Fig. 1. Schematic of the flow geometry, the coordinate system and variables characterizing the deformation of a film flowing over a substrate with 2D topography.

$l_3 = \tilde{L}_3/\tilde{H}_o$ and $d = \tilde{D}/\tilde{H}_o$; d denotes the dimensionless trench depth and takes negative values since the origin of the Cartesian system has been set at the level of the wall surface at the entrance of the domain.

The flow is governed by the momentum and mass conservation equations, which in dimensionless form are:

$$Re\,\underline{u}\cdot\underline{\nabla}\,\underline{u} + \underline{\nabla}P - St\,\underline{g} - \underline{\nabla}\cdot\underline{\underline{\tau}} = 0 \tag{1}$$

$$\underline{\nabla}\cdot\underline{u} = 0 \tag{2}$$

where $\underline{\nabla}$ denotes the gradient operator for Cartesian coordinates, $\underline{u} = (u_x, u_y)$, and P are the velocity vector and the pressure, respectively; $\underline{g} = (\sin a, -\cos a)$ denotes the dimensionless gravity acceleration vector. The extra stress tensor, $\underline{\underline{\tau}}$ is split into a purely viscous part, $2\beta\underline{\underline{\dot{\gamma}}}$, and a polymeric contribution, $\underline{\underline{\tau}}_p$:

$$\underline{\underline{\tau}} = 2\beta\underline{\underline{\dot{\gamma}}} + \underline{\underline{\tau}}_p, \tag{3}$$

where $\underline{\underline{\dot{\gamma}}}$ is the rate-of-strain tensor defined as

$$\underline{\underline{\dot{\gamma}}} = \frac{1}{2}\left(\underline{\nabla}\,\underline{u} + \underline{\nabla}\,\underline{u}^T\right). \tag{4}$$

To describe the rheology of the viscoelastic fluid we employ the affine ePTT model [32,33],

$$\exp\left[\frac{\varepsilon}{1-\beta}De\,tr\underline{\underline{\tau}}_p\right]\underline{\underline{\tau}}_p + De\left(\underline{u}\cdot\underline{\nabla}\,\underline{\underline{\tau}}_p - \underline{\nabla}\,\underline{u}^T\cdot\underline{\underline{\tau}}_p - \underline{\underline{\tau}}_p\cdot\underline{\nabla}\,\underline{u}\right) = 2(1-\beta)\underline{\underline{\dot{\gamma}}}. \tag{5}$$

The viscoelastic fluid properties depend on the dimensionless parameters, De, β and ε. Finite values of the parameter ε impose an upper limit to the elongational viscosity, which increases as this parameter decreases, while it introduces elongational and shear thinning in the fluid model.

The above equations are solved following the EVSS-G method [34,35], which splits the polymeric part of the extra stress tensor into a purely elastic, $\underline{\underline{\Sigma}}$, and a viscous part:

$$\underline{\underline{\tau}}_p = \underline{\underline{\Sigma}} + 2(1-\beta)\underline{\underline{\dot{\gamma}}}, \tag{6}$$

and introduces an independent (continuous) interpolation, $\underline{\underline{G}}$, of the components of the velocity gradient tensor

$$\underline{\underline{G}} = \underline{\nabla}\,\underline{u}, \tag{7}$$

wherever the latter arises in the constitutive equation.

In terms of boundary conditions, along the free surface of the film the velocity field should satisfy a local force balance between capillary forces, stresses in the liquid and pressure in the surrounding fluid and the velocity component normal to this free surface is zero. On the walls of the substrate we impose the usual no-slip and no-penetration conditions. We also impose periodic boundary conditions between the entrance and exit of the flow domain on all primary variables: both streamwise and normal velocity components, pressure, fluid/air interface, velocity gradients and the polymeric part of the stresses. Note that film height at both the inlet and outlet boundaries is set equal to 1 due to our choice of characteristic variables.

It is important to note that, in general, the flow field will deviate from the classical Nusselt flat film solution even in the entrance. Hence, the numerical solution will determine the dimensional film velocity and height in the entrance and from them the Stokes number, St, which appears in the momentum balance. In other words, St is not a parameter of our model but has to be determined as part of the solution by requiring that the average film velocity is equal to unity since the mean velocity at the inflow boundary, $\tilde{U}$, is used as a characteristic velocity for making the model equations dimensionless. Therefore, the additional equation that arises is

$$\bar{u}_x = \int_0^1 u_x dy = 1. \tag{8}$$

In order to solve numerically the above set of equations we have followed the procedure described in Pavlidis et al. [7]). More specifically, the mixed finite element method is used to discretize the velocity, velocity gradient, pressure and stress fields, combined with streamwise upwinding for the constitutive equations and an elliptic grid generation scheme for the discretization of the deformed physical domain (see Dimakopoulos and Tsamopoulos [36]). The generated mesh is refined locally around the convex corners of the topography, as described in Chatzidai et al. [37].

3. Comparison with 2D solutions for Newtonian film flow

Our creeping flow results for Newtonian fluids have been validated already in Pavlidis et al. [7], since they were found to quantitatively agree with the boundary integral solutions obtained by Mazouchi and Homsy [13]. Here we extend this validation to finite Re by first comparing our results for a Newtonian fluid ($De = 0$) with the predictions provided by Gaskell et al. [21] for $Re = 6.67$, $d = -2$, $l_1 = l_2 = l_3 = 40$ and $a = 90^o$.

Fig. 2a shows that the calculated film shapes for two different values of Ca coincide with theirs. Secondly, we compare our predictions for even larger Re with those obtained by Bontozoglou and Serifi [26] for films over topography with isolated step changes for $a = 90^o$. To enable a direct comparison with their results for isolated steps and prevent higher inertia from affecting the periodic boundary conditions, we increased the length of our topography to $l_1 = l_2 = l_3 = 40$ for the smaller Re values and to $l_1 = l_2 = l_3 = 60$

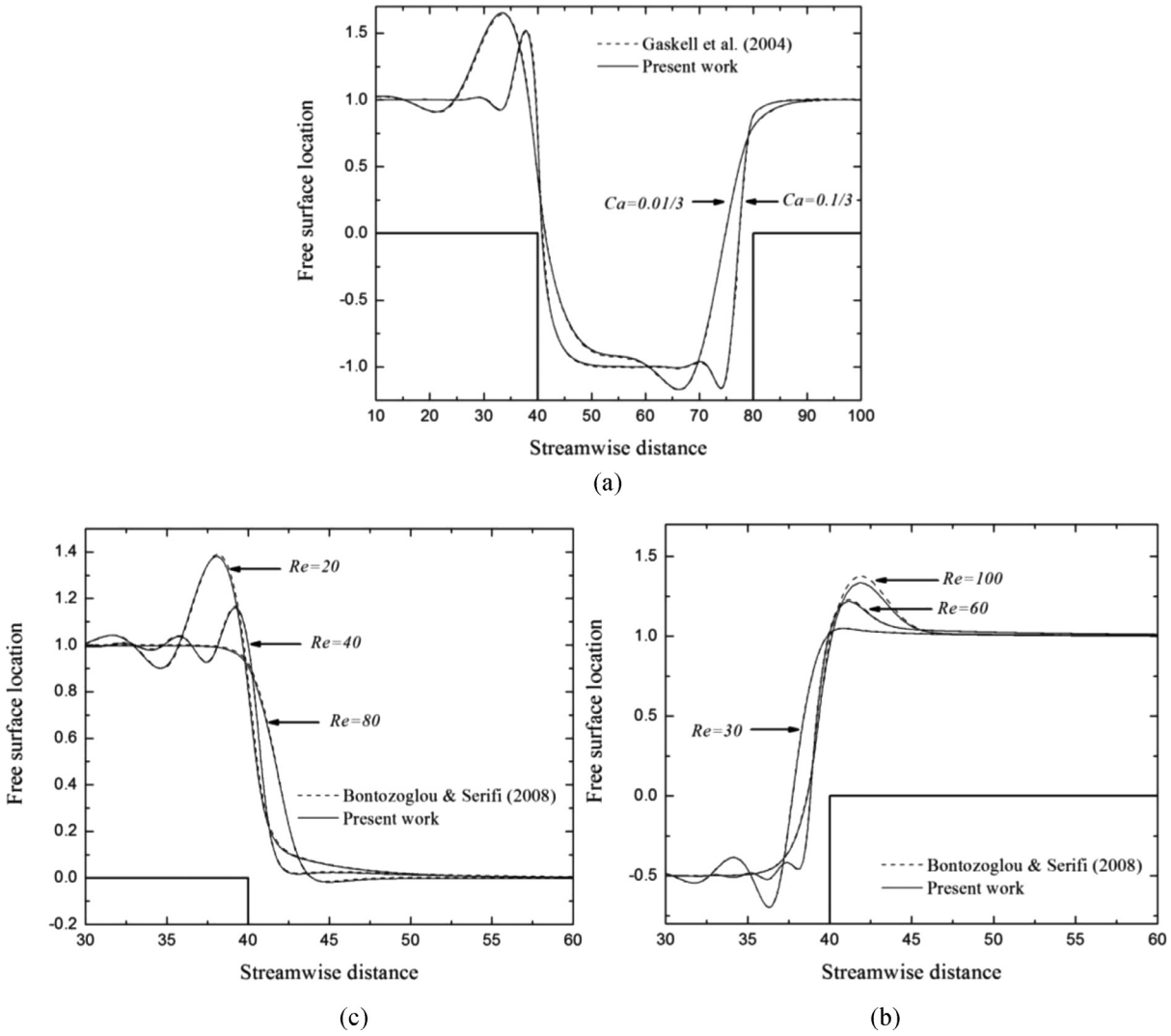

Fig. 2. Comparison of our predictions for a vertically inclined substrate ($a = 90^o$) with previous studies by Gaskell et al. [21] (a) for $Re = 6.67$ and (b) by Bontozoglou and Serifi [26] for various Reynolds numbers at a step down or (c) at a step up for $Ca = 0.025$.

for $Re = 60$ or 100. In Fig. 2b our calculated film profiles are superimposed to those in Bontozoglou and Serifi [26] for a step down with $Ca = 0.025$ and $d = -1$ for various Re, while in Fig. 2c we present a similar comparison for a step up with $d = -1.5$. Our computations are in excellent agreement with those in Bontozoglou and Serifi [26] up to $Re = 60$, while some deviation is observed for $Re = 100$ only around the ridge formed over the step up. The reason for this deviation is unclear. It is certain however, that we have used a much finer mesh than the one used in Bontozoglou and Serifi [26], which we have further locally refined around the convex corners and that we have used a long enough distance from the geometry corners to the inflow and outflow boundaries.

4. Results and discussion

Typical values of the various dimensional quantities in relevant applications (Mazouchi and Homsy [13], Kalliadasis et al. [15], Fraysse and Homsy [20], Bontozoglou and Serifi [26], Saprykin et al. [27]) are $\tilde{\mu} = 1 - 5000cp$, $\tilde{\sigma} = 20 - 50dyn/cm$, $\tilde{\rho} \approx 10^3 kg/m^3$, $\tilde{H}_o = 0.5\mu m - 1mm$, $\tilde{L}_2 = 1\mu m - 1mm$, $|\tilde{D}| = 1\mu m - 1mm$, $\tilde{U} = 10^{-3} - 10^3 cm/s$, $\tilde{\lambda} = 10^{-3} - 1s$, which result in the following values for the dimensionless parameters: $Ca = 10^{-7} - 3$, $Re = 10^{-3} - 400$, $De = 10^{-5} - 10^2$, $l_2 = 1 - 10^3$ and $|d| = 0.1 - 10^2$. The numerical solutions that will be presented below cover a wide range of these parameter values. Since the effect of the rheological parameters ε and β has been discussed in detail by Pavlidis et al. [7], we will keep these values constant, i.e. $\varepsilon = 0.05$, $\beta = 0.1$, and focus our attention on the remaining parameters of our model. This set of parameters corresponds to a liquid that exhibits the effect of shear thinning as well as an extensional viscosity which is varying with extensional hardening followed by extensional thinning for high values of De. For the substrate topography we choose a representative 'base' case with $l_1 = l_3 = 30$, $l_2 = 20$ and $d = -1$, unless otherwise noted. The entrance and exit lengths are larger than in our previous study (Pavlidis et al. [7]) to ensure that, in spite of the much smaller values of the capillary number used here, the flow is fully developed both at the inlet and outlet boundaries.

In the results that will follow, the film will be characterized by certain features, which can be easily quantified for comparing the effect on it of various flow and fluid parameters. In particular, before a step down a capillary ridge is formed and before a step up a capillary depression arises. An important feature of the film is the height of the capillary ridge, $h_{cr} = \tilde{H}_{cr}/\tilde{H}_o$, and the y-position of the capillary depression, $h_{cd} = (\tilde{H}_{cd} - |\tilde{D}|)/\tilde{H}_o$; see Fig. 1. An additional feature is a second ridge that appears above the step up,

created by inertia, the height of which is denoted by $h_{ir} = \tilde{H}_{ir}/\tilde{H}_o$. These features of the film have been used often in the literature [13,15,26].

4.1. Scaling laws

In this section, we will investigate the effect of gravity, elastic, capillary and inertia forces on the flow characteristics by invoking simple scaling arguments. As it will be shown, the approach of [13,15,26] can be extended to take into account the effect of elasticity in order to predict the streamwise length of the capillary features of the film. In order to be able to write an order-of-magnitude estimate of the streamwise momentum balance it is necessary to derive proper scales for the velocity, pressure and stresses.

The characteristic scale for the velocity is based on the classical Nusselt solution for flow along a flat and vertical wall and it is taken to be equal to the mean velocity, $U = \rho g H^2/(3\mu)$. The scale for the pressure disturbance can be obtained by balancing the pressure to the usual interface curvature times the surface tension as it appears in the normal stress balance, $p \approx \sigma \partial^2 h/\partial x^2$. Regarding the stresses, in order to derive their characteristic scales it is necessary to distinguish between the cases of creeping and inertial flow.

4.1.1. Creeping flow

When the effect of inertia is negligible, it is possible to derive the characteristic scales for the stresses by examining the predictions of lubrication theory along the capillary features for a UCM liquid ($\varepsilon = \beta = 0$) (see Saprykin et al. [27]). The shear stress profile is prescribed mainly by the Newtonian part of the flow and therefore for a vertically positioned surface, at leading order, it is determined as follows

$$\tilde{\tau}_{p,xy} \approx (\tilde{p}_x - \rho g)(\tilde{y} - \tilde{h}), \tag{9}$$

The normal xx-component of the polymeric stress, on the other hand, arises at the next order and is given by the following expression

$$\tilde{\tau}_{p,xx} \approx 2\lambda \frac{\partial \tilde{u}_x}{\partial \tilde{y}} \tilde{\tau}_{p,xy}. \tag{10}$$

Using the above expressions and denoting with $\tilde{H}_c$ the height of the capillary features, which is taken to be at most comparable to the local film height, $\tilde{H}_c \approx \tilde{H}$, and $\tilde{L}$ their streamwise length, we end up with the following scales for the pressure and polymeric stresses

$$\tilde{p} \sim \frac{\tilde{\sigma}\tilde{H}}{\tilde{L}^2},\ \tilde{\tau}_{p,xy} \sim \frac{\tilde{\sigma}\tilde{H}^2}{\tilde{L}^3},\ \tilde{\tau}_{p,xx} \sim 2\frac{\tilde{\lambda}\tilde{U}}{\tilde{H}}\frac{\tilde{\sigma}\tilde{H}^2}{\tilde{L}^3} = 2De\frac{\tilde{\sigma}\tilde{H}^2}{\tilde{L}^3}. \tag{11}$$

In our previous study (Pavlidis et al. [7]) it was found that at intermediate to large values of De the capillary ridge gets higher and broader and in this sense, elasticity affects the film in the same way as capillarity. The physical mechanism leading to these changes is the following: inside the ridge, the streamlines are curved and this leads to the development of hoop elastic stresses, due to the stretching of molecules, acting towards the center of curvature and thus working cooperatively with the capillary pressure to drive liquid in the transverse direction towards the trench. These two forces must be sufficient to balance the combined effect of gravity and inertia which drive liquid in the streamwise direction. Taking this into account along with the scales discussed above, we write the following order-of-magnitude estimate of the streamwise momentum balance

$$\tilde{\rho}\tilde{g} \approx \frac{\tilde{\sigma}\tilde{H}}{\tilde{L}^3} + 2De\frac{\tilde{\sigma}\tilde{H}^2}{\tilde{L}^4} \Rightarrow 3l^3 \approx \frac{1}{Ca} + 2\frac{De}{Ca}l^{-1}, \tag{12}$$

where elasticity and capillary pressure balance the effect of gravity. Here $l = \tilde{L}/\tilde{H}$ denotes the dimensionless streamwise scale of the capillary features. As discussed in Bontozoglou & Serifi [26], the influence of viscous forces that appears to be neglected in the above balance is actually hidden in the definition of the velocity scale, U.

From Eq. (12) it is possible to identify 2 different limiting regimes

I. capillary-gravity regime

$$\left(De \ll Ca^{-1/3}\right) : l \sim Ca^{-1/3} \tag{13}$$

II. elasticity-gravity regime

$$\left(De \gg Ca^{-1/3}\right) : l \sim \left(\frac{De}{Ca}\right)^{1/4} \tag{14}$$

The first regime (I.) is identical to the one that has already been identified by Kalliadasis et al. [15] and Bontozoglou & Serifi [26] in the case of a Newtonian fluid. When, however, the flow is dominated by the elasticity of the material, and therefore the capillary effects can be neglected, another regime arises (II.), where gravity is balanced by elasticity. By equating the two terms of the right hand side of Eq. (12), it is possible to derive a criterion for the transition from the capillary-gravity regime to the elasticity-gravity regime. Doing so, we find that the two terms balance when $l = 2De$ and by substituting back this value we end up with the following expression for the transition Deborah number

$$De_t = \left(\frac{1}{12Ca}\right)^{1/3}. \tag{15}$$

4.1.2. Inertial flow

In order to derive the characteristic scales for the stresses in the presence of finite inertia, we examine again the case of a UCM liquid ($\varepsilon = \beta = 0$) following however a similar methodology to the one that has been described in the works of Benney [38], Krantz & Goren [39] and Atherton & Homsy [40] for a Newtonian liquid, i.e. by expressing the velocity in terms of a stream function and using a long wave perturbation expansion (i.e. assuming disturbances with aspect ratio (height/length) $\delta \ll 1$). It is found that the shear stress profile is again prescribed mainly by the Newtonian part of the flow which is now given by the following expression at leading order

$$\tilde{\tau}_{p,xy} \approx \rho g(\tilde{y} - \tilde{h}), \tag{16}$$

The above expression has been derived assuming that the Weber number ($We = \tilde{\rho}\tilde{U}^2\tilde{H}_o/\tilde{\sigma}$) is of the order $We \sim O(\delta^2)$. Under this condition the effect of surface tension on shear stress, $\tilde{\tau}_{p,xy}$, becomes subdominant, therefore arising at the next order (see Atherton & Homsy [40]). Such an assumption is not unreasonable and corresponds for instance to the cases shown in Fig. 2a taking as δ the aspect ratio of the capillary ridge. The normal xx-component of the polymeric stress arises at the next order and is given by

$$\tilde{\tau}_{p,xx} \approx 2\lambda \frac{\partial \tilde{u}_x}{\partial \tilde{y}} \tilde{\tau}_{p,xy}. \tag{17}$$

Using the above expressions and denoting with $\tilde{H}$ the height of the capillary features and $\tilde{L}$ their streamwise length, we end up with the following scales for the pressure and polymeric stresses

$$\tilde{p} \sim \frac{\tilde{\sigma}\tilde{H}}{\tilde{L}^2},\ \tilde{\tau}_{p,xy} \sim \tilde{\rho}\tilde{g}\tilde{H},\ \tilde{\tau}_{p,xx} \sim 2De\tilde{\rho}\tilde{g}\tilde{H}. \tag{18}$$

Now, assuming that the flow is dominated by inertia it is possible to write the following order-of-magnitude estimate of the streamwise momentum balance

$$\frac{\tilde{\rho}\tilde{U}^2}{\tilde{L}} \approx \frac{\tilde{\sigma}\tilde{H}}{\tilde{L}^3} + 2De\frac{\tilde{\rho}\tilde{g}\tilde{H}}{\tilde{L}} \Rightarrow Rel^2 \approx \frac{Re}{We} + 6Del^2, \tag{19}$$

where the combined effect of elasticity and capillary pressure balance the effect of inertia. For negligible elasticity, inertia is balanced by the effect of surface tension and in this case we are able to reproduce the regime that has been identified by Bontozoglou & Serifi [26] in the case of a Newtonian fluid ($l \approx We^{-1/2}$). On the other hand, for an elastic liquid and in the limit $De \ll Re$, it is possible to derive from Eq. (19) the following expression for the streamwise lengthscale

$$l \approx We^{-1/2}\left(1 + \frac{3De}{\mathrm{Re}}\right), \tag{20}$$

which suggests that the lengthscale increases with *De*. We also observe in Eq. (19) that the streamwise length, *l*, is raised to the same exponent in the inertia and elastic terms which indicates that *l* does not scale to some power of *De* and therefore should not depend strongly on the level of the material elasticity.

The scaling arguments that have been presented here both for creeping flow conditions and inertial flow will be checked against our numerical results that will be presented below.

4.2. Effect of surface tension

We begin our numerical study by examining the case of a viscoelastic film with $De = 2$, under creeping flow conditions ($Re = 0$), for various values of the *Ca* number. We also consider that the substrate is vertically oriented ($a = 90^o$). Regarding the computed value of the *St* number, it should be mentioned that it does not vary with *Ca* and its dependence on *De* has been given in Fig. 14 of Pavlidis et al. [7]. The free surface profiles are depicted in Fig. 3a, while the dependence of the most important film features, i.e. the heights of the capillary ridge, h_{cr}, and the capillary depression, h_{cd}, on *Ca* are plotted in Fig. 3b. The capillary ridge height monotonically decreases with increase of *Ca*, whereas the height of the capillary depression first decreases and then increases with *Ca*. Moreover, both appear to move upstream, away from the topographical feature, and the film variation around them becomes broader. We also note that, for high values of *Ca,* the shape of the liquid-gas interface follows more closely the topography of the substrate; the opposite is true for low *Ca* values. The physical mechanism leading to these changes is the following: The increased capillary force smooths out the film interface inside the trench. This leads to the upstream movement of the capillary depression and to the merging of the initially distinct concave corners of the free film surface to a single but deeper depression. When this starts occurring, the flow in the middle of the cavity ceases to be fully developed, in spite of its length, and the film variations around the step down and the step up are no longer independent from each other. As long as the film depression remains closer to the step up its amplitude increases with decreasing *Ca*, but when it gets further away from it reaching the middle of the trench, its amplitude starts to decrease with decreasing *Ca*, because now capillarity more effectively smooths out the film/air interface. Turning now into the capillary rise before the step down, the smoothening of the film inside the trench as *Ca* decreases makes necessary an increased maximum height of the ridge in order to maintain the pressure difference generated by capillarity, which changes the flow direction of the film and drives it inside the trench.

In general, capillarity is seen to act in the same way as with Newtonian fluids, but the presence of viscoelasticity intensifies its effects and maintains them for larger values of *Ca*. In Fig. 3b we observe that the height of the capillary ridge monotonically decreases with increasing *Ca* and at a value of *Ca* that depends on *De* it becomes zero. For small values of *De* this occurs at a specific value of *Ca* (h_{cr} becomes equal to unity at $Ca \approx 0.55$, 0.77 and 1.20 for $De = 0$, 0.5 and 1, respectively), whereas for larger values of *De* the height of the capillary ridge decreases asymptotically to unity (see Fig. 3c). Apparently, in the case of highly elastic liquids the ridge is maintained even for large values of *Ca*. In terms of the planarization efficiency this behaviour implies that in order to achieve an unperturbed film thickness just before the step down for materials with increasing elasticity (increasing *De*) it would be necessary to increase the value of *Ca* as much as possible. Regarding the capillary depression, the variation of h_{cd} is similar for the two values of *De* in this figure, but *De* decreases the capillary depression for the smaller values of *Ca*.

The effect of viscoelasticity on the film features is also depicted in Fig. 4a and 4b where we plot the variations of the maximum ridge height, h_{cr}, and the minimum *y*-position of the capillary depression, h_{cd}, as a function of *De* with *Ca* as a parameter. In our previous study (Pavlidis et al. [7]) it was shown that for small levels of fluid elasticity, h_{cr} decreases with *De* due to the effect of fluid elasticity and more specifically the presence of primary normal stress, $\tau_{p,\,xx}$, in the vicinity of the step down (see also Saprykin et al. [27]). However, above a certain value of *De*, shear and elongational thinning become important leading to a reduction of the polymeric stresses and this in turn leads to increase of the ridge height with *De*. As it is shown in Fig. 4a, this non-monotonic dependence exists for all *Ca* that have been examined, albeit it becomes weaker for high values of *Ca*; the ridge height decreases significantly in the high *Ca* regime and thus its dependence on *De* also decreases for low elasticity. We also note that the critical value of *De* for which the monotonicity changes depends on *Ca*, moving towards smaller values with decreasing surface tension. The picture is somewhat more complex for the capillary depression, h_{cd}, shown in Fig. 4b. In the low *De* regime, h_{cd} weakly increases with *De* whereas in the case of high elasticity the depression may either deepen for large *Ca* values or decrease its depth for small *Ca*. Interestingly, for highly elastic liquids, h_{cd} may even acquire positive values for $Ca = 0.01$ which indicates that in this case the free surface exhibits very little conformance to the topography.

As it was discussed in Section 4.1, under creeping flow conditions and for highly elastic liquids, the flow in the *x*-direction is driven by gravity and it is balanced by the liquid elasticity which drives the liquid inside the trench. In this elasticity-gravity regime the streamwise length-scale of the ridge before the step down was shown to scale as $l \sim (\frac{De}{Ca})^{1/4}$. In order to check the above scaling estimate, we compare it against our numerical results presented above. For the evaluation of the streamwise length scale, *l*, we adopt the same definition with Bontozoglou & Serifi [26], i.e. the horizontal distance defined by the intersection of the unperturbed film surface (at $y = 1$) with the two tangents to the main ridge before the step down at the locations of maximum absolute slope. The values of *l* calculated following the above procedure are plotted in Fig. 5a as a function of *De* for different values of *Ca*. Indeed, the numerical data confirm the existence of a power law with exponent 1/4 in the high *De* regime verifying the above asymptotic limit. The dependence of *l* on *Ca* is also evident in this figure. By taking into account that in the limit of a Newtonian fluid ($De = 0$) the lengthscale varies as $l_{newt} \sim Ca^{-1/3}$, the above scaling estimate for the elastic liquid can be rewritten in terms of the normalized lengthscale as $l/l_{newt} \sim (DeCa^{1/3})^{1/4}$. Interestingly, plotting l/l_{newt} against $DeCa^{1/3}$ in Fig. 5b we find that the different curves almost collapse to one thus corroborating the validity of our analysis. Finally, according to Eq. (15) the transition from the capillary-gravity regime to the elasticity-gravity regime takes place for $De_tCa^{1/3} \approx (1/12)^{1/3}$, indicated with a vertical line in Fig. 5b.

4.3. Effect of inertia

We continue our study with the investigation of the interaction of fluid inertia with viscoelasticity and how it may affect the

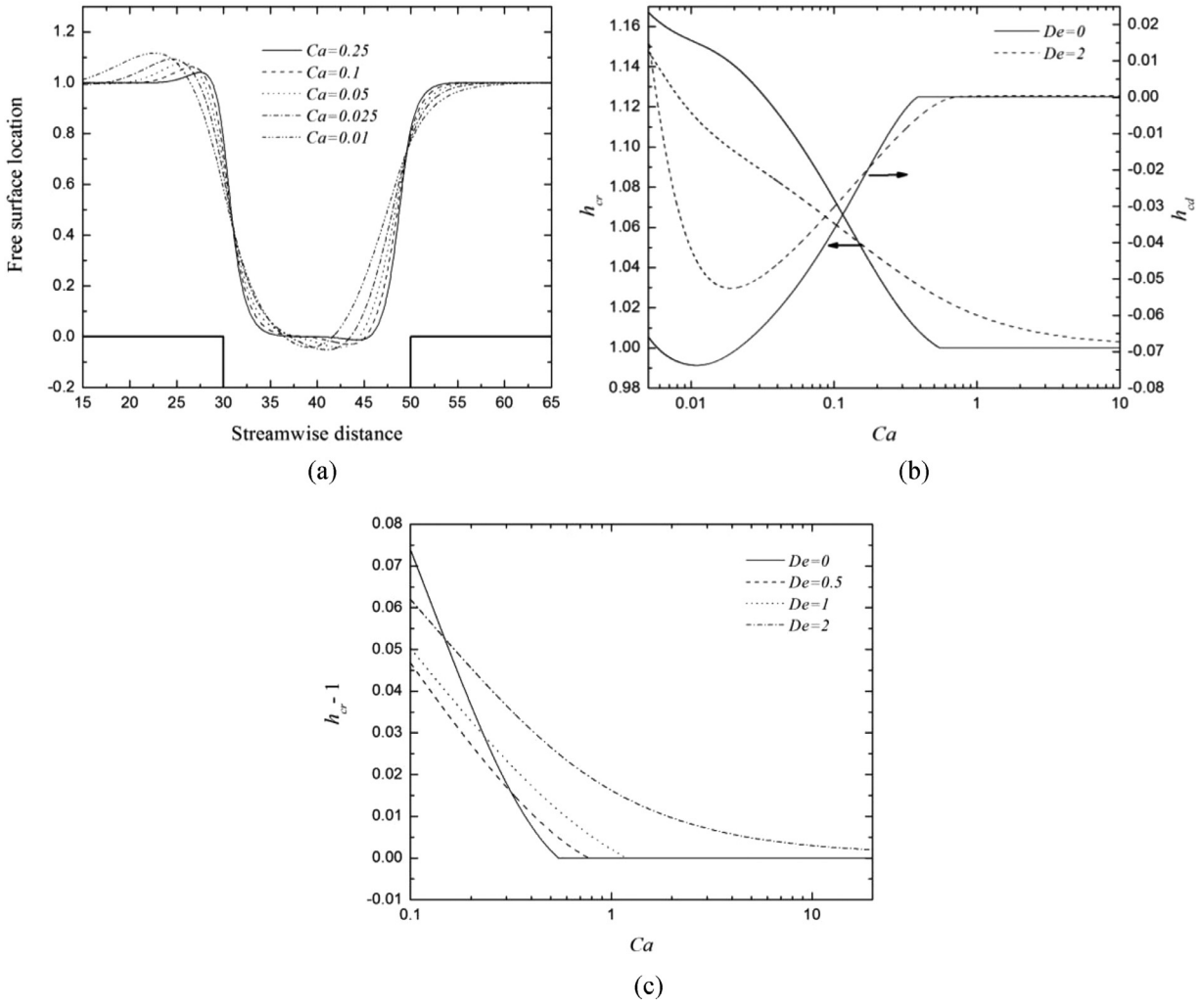

Fig. 3. (a) Profiles of the calculated free surfaces for $De = 2$ and various Ca. Dependence of (b) h_{cr} and h_{cd} and (c) the net deviation height, $h_{cr} - 1$ on Ca for various values of De. The remaining parameters are $Re = 0$, $\varepsilon = 0.05$, $\beta = 0.1$, $l_1 = l_3 = 30$, $l_2 = 20$, $d = -1$, $a = 90^o$.

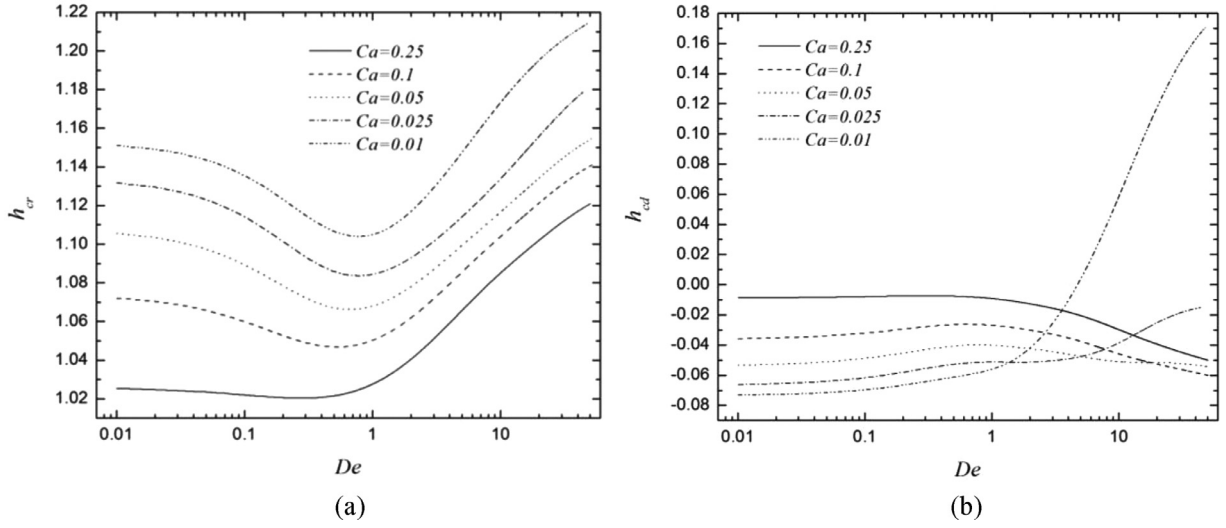

Fig. 4. Dependence of (a) h_{cr} and (b) h_{cd} on De for various Ca. The remaining parameters are $Re = 0$, $\varepsilon = 0.05$, $\beta = 0.1$, $l_1 = l_3 = 30$, $l_2 = 20$, $d = -1$, $a = 90^o$.

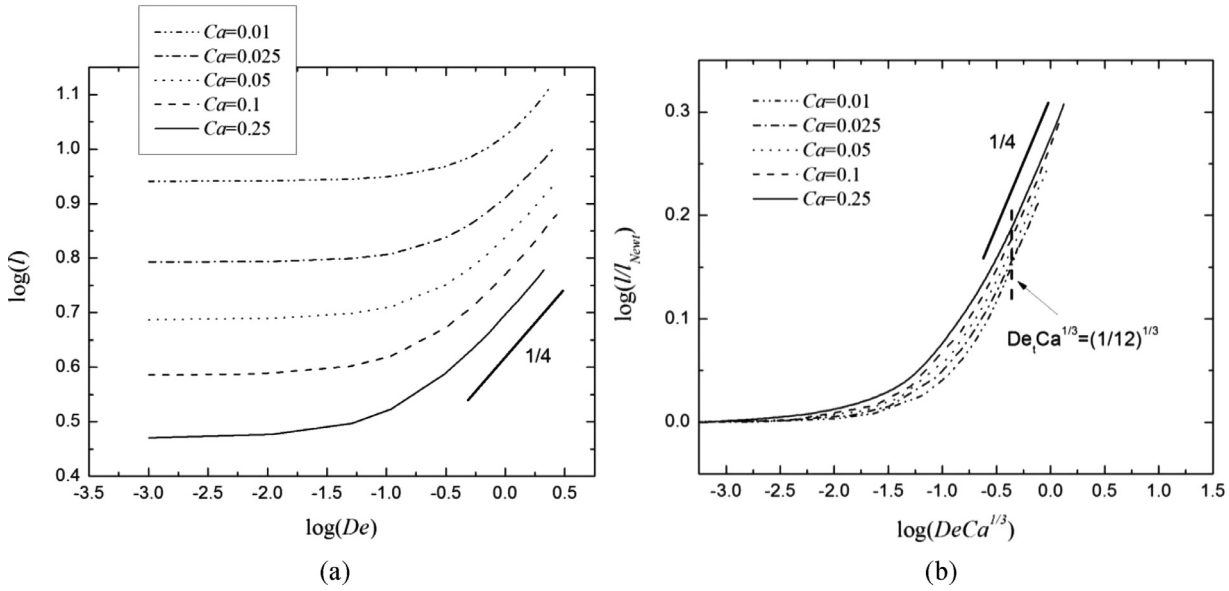

Fig. 5. Variation of (a) the streamwise lengthscale, l, on De and (b) the normalized streamwise lengthscale, l/l_{newt}, on $DeCa^{1/3}$. The remaining parameters are $Re = 0$, $\varepsilon = 0.05$, $\beta = 0.1$, $l_1 = l_3 = 30$, $l_2 = 20$, $d = -1$, $a = 90^o$.

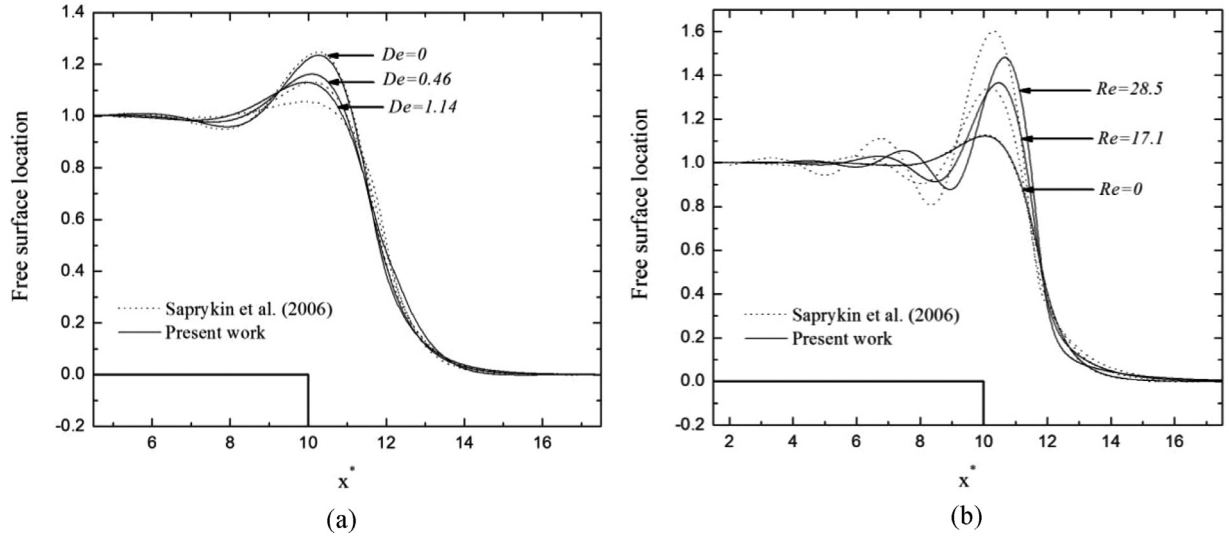

Fig. 6. Comparison of our predictions with previous study by Saprykin et al. [27] for (a) various Deborah numbers when $Re = 5.69$ and (b) various Reynolds numbers when $De = 0.23$ at a vertically oriented isolated step ($d = -1$, $a = 90^o$).

resulting flow field. Before we proceed further it is useful to compare first our 2D numerical simulations for finite inertia against the predictions of Saprykin et al. [27] who employed the lubrication theory in the limit of $De << 1$, while adopting the Maxwell model to describe the fluid rheology. In Fig. 6a we depict a comparison of the calculated free surface profiles for the case of an isolated step ($d = -1$) for $\mathrm{Re} = 5.69$ and $Ca = \frac{0.025}{3}$ and three different values of De; note that for comparison purposes the streamwise length in this figure has been scaled with the capillary lengthscale $x^* = xCa^{1/3}$. This figure confirms that for finite inertia and in the limit of small De our results are in good agreement with Saprykin et al. [27]. However, as the elasticity of the material becomes more important, the deviation between the two approaches appears to increase significantly and as it is shown for $De = 1.14$ the lubrication approximation considerably underestimates the size of the capillary features. In order to evaluate how the validity of long-wave theory depends on Re we fix De to a small value ($De = 0.23$) and compare in Fig. 6b the solutions for a wide range of Re values keeping the same flow configuration. Clearly, our results are in excellent agreement at the creeping flow limit, as should be expected, whereas the waves on the interface deviate not only in height but also in modulation as Re increases. These results are hardly surprising since the asymptotic expansion presented by Saprykin et al. [27] is valid under the assumptions of weak inertia and weak viscoelasticity. It is also important to note that one more constraint which arises from the analysis of Saprykin et al. [27] is that their analytical model is valid only for relatively high surface tension values because of the long wave assumption. No such restriction applies in our numerical approach since we solve directly the 2D problem without making simplifications of any kind.

We turn now our attention back to the film flow over a rectangular trench. In Fig. 7 free surface profiles are depicted for a wide range of Re and for $Ca = 0.1$, $De = 2$, $\varepsilon = 0.05$, $\beta = 0.1$, $l_1 = l_3 = 30$, $l_2 = 20$, $d = -1$, $a = 90^o$. For moderate values of Re, we observe a marked departure from the creeping flow limit, since the usual single capillary ridge and depression have been substituted by a wave

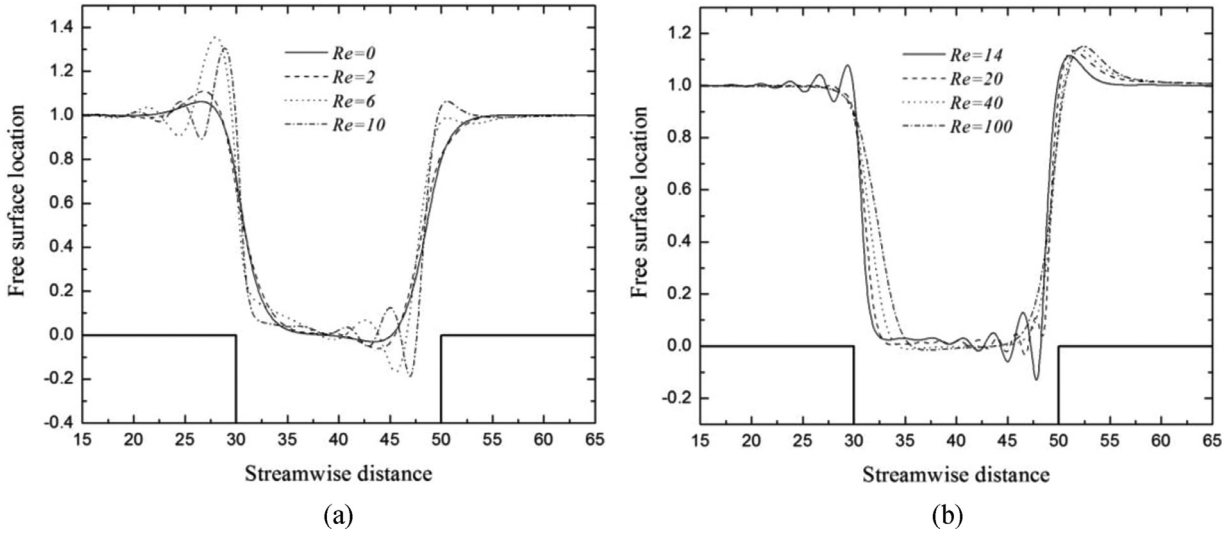

Fig. 7. Profiles of the calculated free surfaces for $De = 2$. The remaining parameters are $Ca = 0.1$, $\varepsilon = 0.05$, $\beta = 0.1$, $l_1 = l_3 = 30$, $l_2 = 20$, $d = -1$, $a = 90^o$ and various Re.

which is spatially damped in the upstream direction in both cases. It has been established already for a Newtonian fluid (see Bontozoglou & Serifi [26]), that inertia apart from giving rise to a ridge above the step up, also generates damped waves that span almost the entire film, in contrast to all other forces and parameters examined so far, which have a local effect on the film. Clearly, this behaviour is retained in the case of a viscoelastic liquid examined here.

It is seen in Fig. 7a that both waves near the step down and the step up cover a larger distance as Re increases up to ~6, while their maximum moves downstream and increases in amplitude. At even larger values of Re, Fig. 7b, the location of their maximum remains fixed and decreases in magnitude until they disappear for very high values of Re. On the other hand, the elevation of the free surface which occurs immediately after the step up, hereafter referred as the inertial ridge, appears to move downstream and grow in size with increasing Re as in the case of Newtonian liquids. As it will be shown below the presence of viscoelasticity intensifies the characteristics of these features.

The parametric variation of the flow characteristics with Re and De numbers is shown in detail in Fig. 8. More specifically, Fig. 8a shows the dependence of the Stokes number, which is calculated as part of the solution using Eq. (8), on Re for various De, while $Ca = 0.1$, $\varepsilon = 0.05$, $\beta = 0.1$, $l_1 = l_3 = 30$, $l_2 = 20$ and $d = -1$. The Stokes number decreases with increasing De due to the effect of shear thinning, introduced by the parameter ε, but has a rather weak dependence on the Reynolds number. Regarding the characteristics of the various interfacial features, we depict in Fig. 8b the dependence of the net height of the capillary ridge, $h_{cr} - 1$, on Re for various De. The height of the most prominent ridge near the step down obtains its maximum value for intermediate Re values, having a non-monotonic dependence with De, while for higher Re it drops to the unperturbed thickness. As the material becomes more elastic, the maximum height of this ridge increases while the transition to an unperturbed film thickness for higher Re becomes steeper. A similar behavior is also found for the capillary depression which becomes deeper with increasing material elasticity; this is shown in Fig. 8c. Its amplitude is also maximized at moderate Re (i.e. $Re < 20$) whilst for larger Re values, h_{cd} becomes very small and with a rather weak dependence on inertia and elasticity.

The order-of-magnitude analysis presented in Section 4.1 suggests that in the case of inertial flow the streamwise length-scale of the capillary features should not depend strongly on the material elasticity. In order to check this, we plot in Fig. 9a the streamwise length-scale, l, (evaluated from the numerical solution in a similar manner with Fig. 5) as a function of De for $Re = 10$ and $Ca = 0.1$. The dependence of the streamwise lengthscale on the material elasticity is indeed found to be rather weak in direct agreement with the analysis based on simple scaling arguments.

According to Bontozoglou & Serifi [26], in the case of a Newtonian fluid ($De = 0$) the disappearance of the capillary ridge takes place for a constant value of the Weber number, $We = ReCa$, indicating that when this happens inertia dominates over capillary forces. Fig. 9b demonstrates that this is also true in the case of a viscoelastic material, albeit the disappearance of the ridge happens at higher value of the We, since inertia has also to overcome the effect of elasticity.

As it was noted above apart from the disappearance of the capillary ridge, the presence of inertia is also responsible for the formation of a ridge above the step up when Re is large enough. The appearance of this ridge is clearly caused by an overshoot of the liquid film as it is deflected in the horizontal direction by the step; its height is denoted by h_{ir}. Fig. 8d depicts the net height of the inertial ridge, $h_{ir} - 1$, as a function of Re. The inertial ridge arises beyond some critical value of Re, which depends on the level of elasticity of the material, and its size increases up to $Re \approx 20$ for both Newtonian and viscoelastic fluids. Nonetheless, the size of the inertial ridge increases considerably with De, because the polymeric chains try to maintain their configuration and flow direction. In the case of a mildly elastic material ($De = 0.5$) further increase of Re, leads to a decrease of the inertial ridge height reaching the Newtonian limit whereas for the most elastic liquid ($De = 2$), the ridge appears to keep growing with inertia.

In order to visualize the flow inside the cavity we depict the streamlines in Fig. 10 for $De = 2$, $Ca = 0.1$, $\varepsilon = 0.05$, $\beta = 0.1$, $l_1 = l_3 = 30$, $l_2 = 20$, $d = -1$ and $a = 90^o$ and for three different values of Re. Under creeping flow conditions the presence of elasticity gives rise to a recirculation vortex in the downstream corner of the cavity due to the effect of normal stresses; this is a well known property of a viscoelastic fluid when facing an abrupt contraction. Increase of the Reynolds number, however, leads eventually to the suppression of the formed wake whereas on the other side of the rectangular cavity we observe exactly the opposite behavior. At the bottom of the sudden expansion, flow separation occurs for Re = 10 which becomes more prominent with increase of Re.

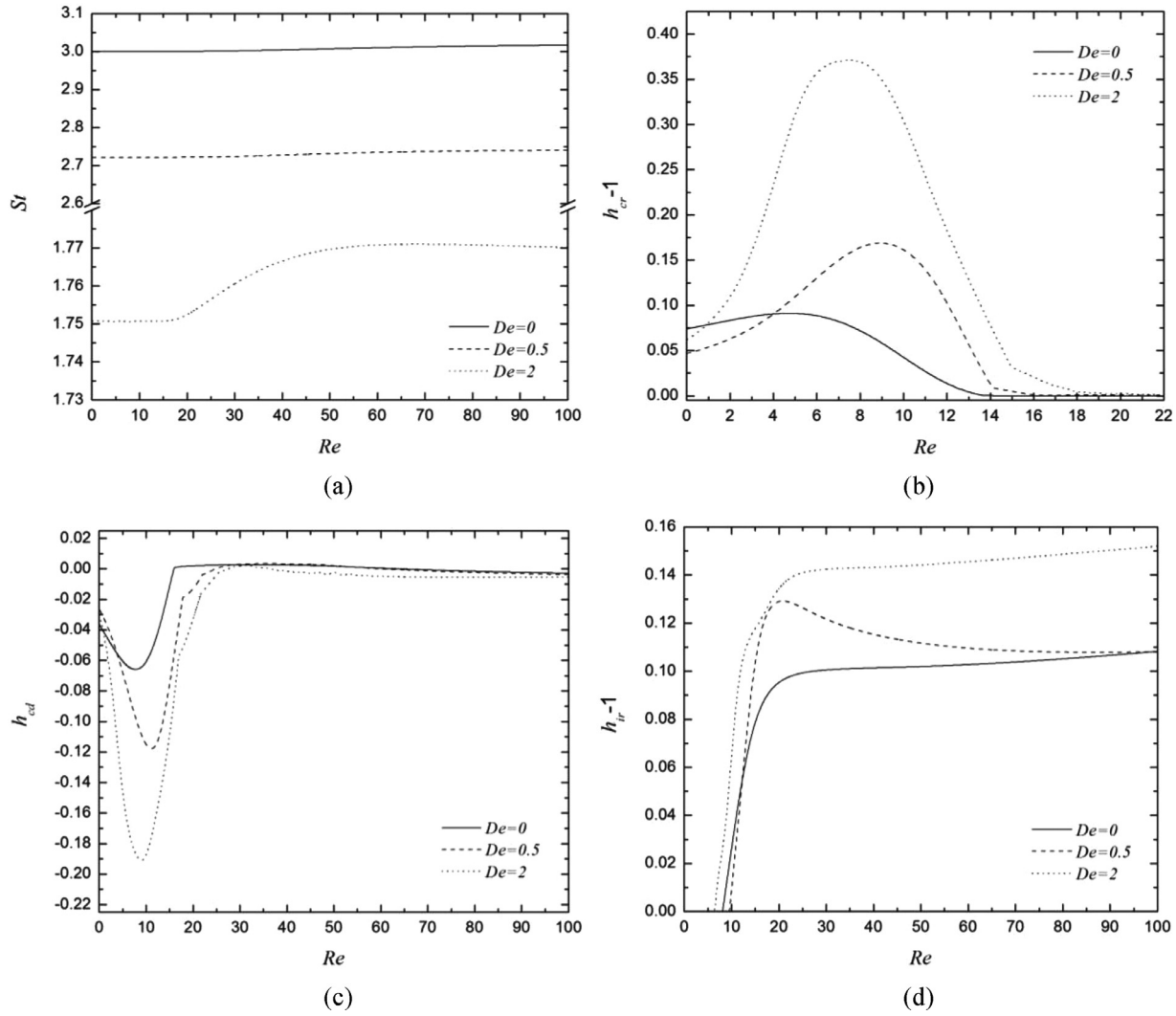

Fig. 8. Dependence of (a) $h_{cr} - h_o$, (b) h_{cd}, (c) $h_{ir} - h_o$ and (d) St on Re for $De = (0,\ 0.5,\ 2)$. The remaining parameters are $Ca = 0.1$, $\varepsilon = 0.05$, $\beta = 0.1$, $l_1 = l_3 = 30$, $l_2 = 20$, $d = -1$ and $a = 90^o$.

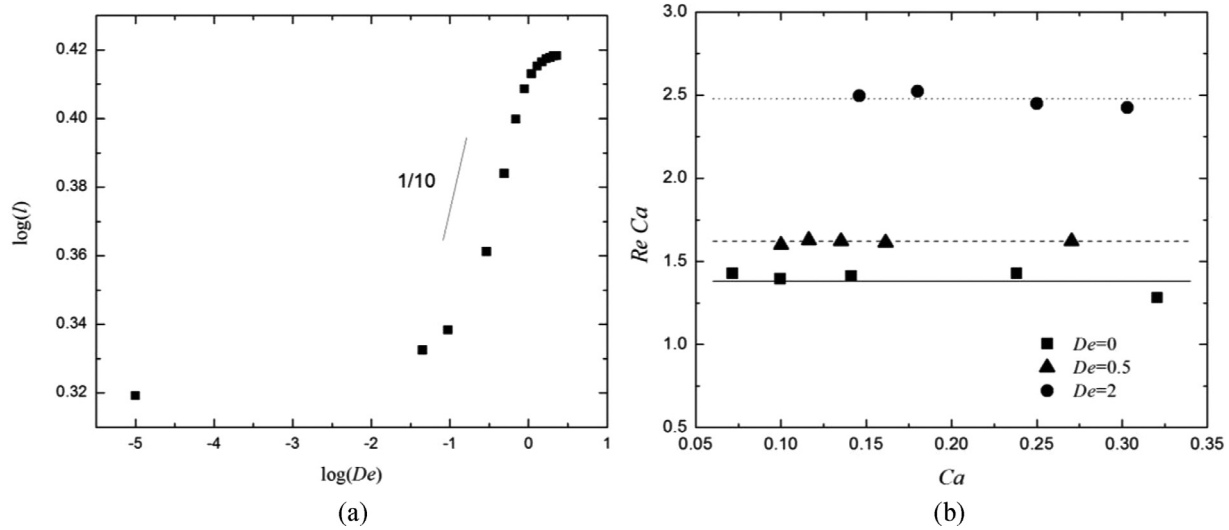

Fig. 9. (a) Dependence of the streamwise length-scale of the capillary ridge on De for $Re = 10$ and $Ca = 0.1$, (b) The conditions where the capillary ridge disappears for $De = (0,\ 0.5,\ 2)$. The remaining parameters are $\varepsilon = 0.05$, $\beta = 0.1$, $l_1 = l_3 = 30$, $l_2 = 20$, $d = -1$ and $a = 90^o$.

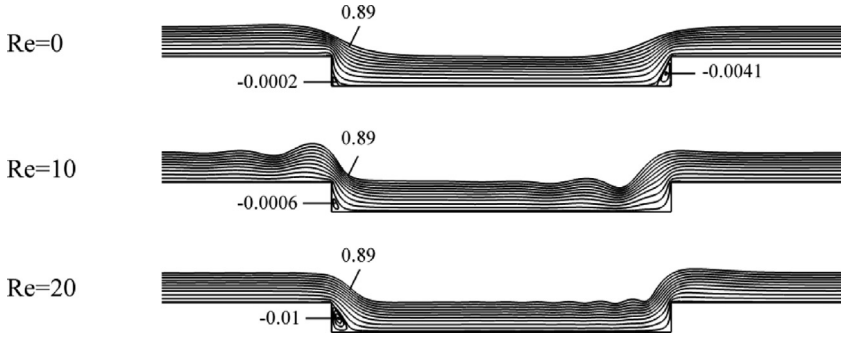

Fig. 10. Streamlines for various values of *Re*. The remaining parameters are $Ca = 0.1$, $De = 2$, $\varepsilon = 0.05$, $\beta = 0.1$, $l_1 = l_3 = 30$, $l_2 = 20$, $d = -1$ and $a = 90^o$.

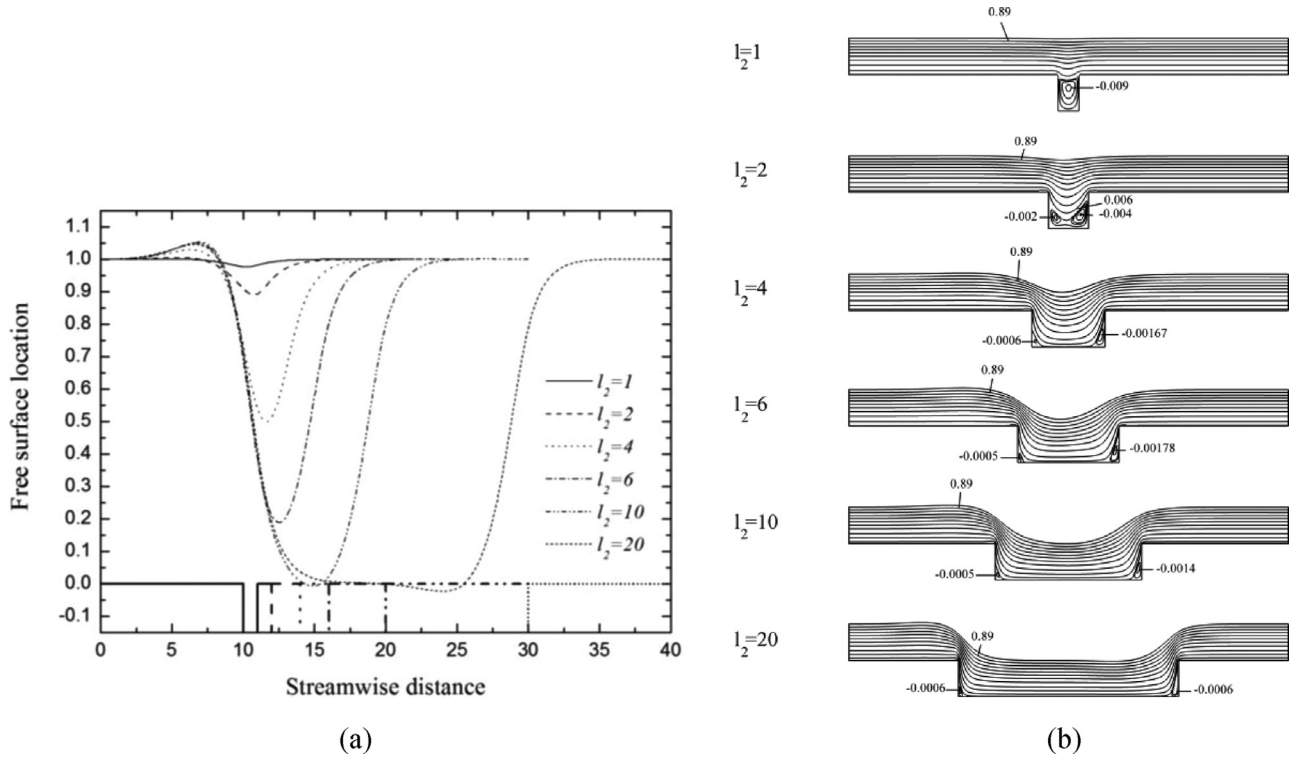

Fig. 11. Dependence of (a) shapes of the predicted free surfaces and (b) streamlines on width, l_2, for $Re = 0$, $Ca = 0.1$, $De = 1$, $\varepsilon = 0.05$, $\beta = 0.1$, $l_1 = l_3 = 10$, $d = -1$ and $a = 90^o$.

4.4. Effect of substrate geometry

We continue our study with the investigation of the effect of the various geometrical characteristics of the substrate topography, i.e. the effect of cavity width, l_2, and depth, d.

4.4.1. Effect of the cavity width, l_2

First we examine in Fig. 11 the effect of the cavity width, l_2 for $Re = 0$, $Ca = 0.1$, $De = 1$, $\varepsilon = 0.05$, $\beta = 0.1$, $l_1 = l_3 = 10$ $d = -1$ and $a = 90^o$. The dependence of the free surface shape on the trench width is shown in Fig. 11a. For cavities with narrow widths (low values of l_2) the interface remains almost unperturbed as less liquid enters in the smaller trench, but flows over it. In Fig. 11b the streamlines are presented and show that in the case of cavity with the smallest width ($l_2 = 1$) the fluid inside the cavity is essentially trapped in this region and a single recirculation vortex covers the whole cavity. As the cavity width increases we find cases ($l_2 = 2$) where a large volume of fluid is entrapped in two separate co-rotating vortices which cover almost the whole bottom region; note that the flow between the vortices is negligibly small. Further increase of the width leads to separation of the two eddy flow structures which remain close to the concave corners.

We observe that as l_2 increases, more viscoelastic fluid enters inside the cavity and this leads to a distortion of the liquid-air interface. This also necessitates the formation of a capillary ridge with larger size, since there is greater need to re-orient the liquid inside the cavity. Moreover, for the greatest examined width, we note the existence of a constant film thickness region inside the trench.

4.4.2. Effect of the cavity depth, d

Fig. 12a shows the dependence of the free surface shape on the trench depth for $Re = 0$, $Ca = 0.1$, $De = 1$, $\varepsilon = 0.05$, $\beta = 0.1$, $l_1 = l_3 = 10$, $l_2 = 20$ and $a = 90^o$. We observe that as the trench depth increases, both the sizes of capillary ridge and depression become more intense. This can be explained by the fact that in deeper cavities, the fluid needs to follow the substrate geometry and to move in the transverse direction for longer distances. The capillary pressure which forces the fluid to move in the normal direction has to increase resulting in more prominent ridges. Similarly, the capillary depression becomes enhanced so that the

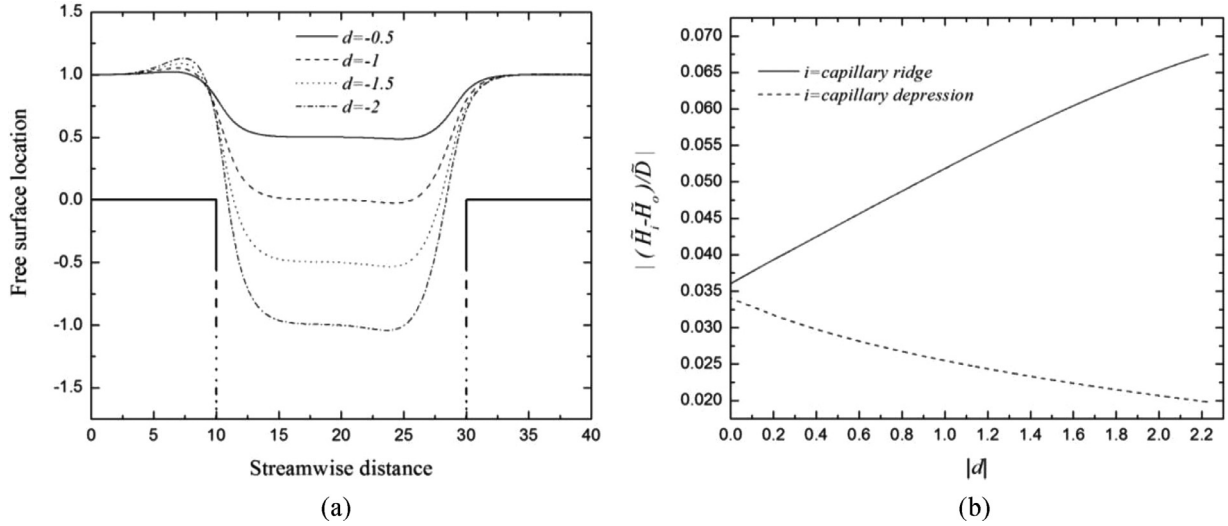

Fig. 12. Dependence of (a) shapes of the predicted free surfaces and (b) deviation heights normalized by the trench depth for $Re = 0$, $Ca = 0.1$, $De = 1$, $\varepsilon = 0.05$, $\beta = 0.1$, $l_1 = l_3 = 10$, $l_2 = 20$ and, $a = 90^o$.

capillary pressure pushes the fluid towards the topography at the step up. This can be seen more clearly in Fig. 12b where we plot the net height of the capillary ridge (solid line) and depression (dashed line) normalized by the trench depth. It is observed that a linear variation exists between depth and these normalized capillary features. Interestingly, these quantities remain unequal even for the case of an infinitesimal depth contrary to the predictions for a Newtonian fluid (Bontozoglou and Serifi [26]) and this effect can be attributed to material elasticity.

4.5. Effect of inclination angle, α

So far we have examined the case of a vertically oriented substrate. It is interesting though to examine the effect of the inclination angle, α, of the solid substrate on the flow of the viscoelastic fluid. In Fig. 13a we plot the free surface profiles for $De = 2$ and various values of α. As the inclination angle departs from the vertical case, the topology of the free surface changes drastically; the ridge before the step down diminishes and the depression before the step up is elevated and moves upstream. This is due to the fact that with decreasing inclination angles the liquid is not driven inside the trench solely due to the effect of the capillary pressure but the latter acts cooperatively with the increasing y-component of gravity and therefore not as large capillary pressure is needed reducing the height of the capillary ridge. The latter is also reflected on the drastic change of the pressure field which is depicted in Fig. 14; as the substrate approaches the horizontal plane, pressure contours are becoming parallel to it. Pressure increases with increasing depth because of the increasing weight of fluid exerting downward force from above. On the contrary in the case of a vertically oriented film the capillary-generated pressure is responsible for driving the liquid inside the cavity.

The dependence of the maximum ridge height, h_{cr}, and depression depth, h_{cd}, on $\alpha$are shown more clearly in Fig. 13b for two different values of De. With decreasing α the height of the capillary ridge, h_{cr}, decreases up to a certain value of inclination angle which depends strongly on De. Decreasing further the inclination angle leads to a change of monotonicity albeit the ridge height remains approximately equal to the unperturbed film thickness. Regarding the capillary depression depth, h_{cd}, we observe an elevation with decreasing αwhich becomes more pronounced in the case of a viscoelastic fluid.

Finally, the dependence of the calculated St number on α is depicted in Fig. 13c. Moving from a vertically oriented film to a horizontal one it is reasonable to expect that the average velocity will decrease. Since St is by definition inversely proportional to the average velocity, this implies that the value of St should increase with a and this is indeed found by our simulations. We observe that in the case of the viscoelastic fluid the rate of increase diminishes as compared to the case of a Newtonian fluid and this is attributed to the shear thinning properties of the viscoelastic material which allows higher flow rates for films of the same height.

5. Conclusions

We have studied the steady film flow of a viscoelastic fluid obeying the PTT constitutive law focusing on the interaction of the effect of material elasticity with the effect of capillary and inertia forces. We solve the 2D problem using the mixed finite element method combined with an elliptic grid generation scheme. The viscoelastic stresses where discretized using the EVSS-G/SUPG method which allowed simulation up to high values of the Deborah number. In order to validate our code we compared our predictions with previous works concerning Newtonian and weakly viscoelastic materials.

It is shown that viscoelasticity and surface tension act in the same way, i.e. capillary waves move upstream and become broader with increasing material elasticity. It appears therefore that the bulk elasticity of the viscoelastic material has a similar effect to surface tension, which can also be interpreted as the elasticity of the interface. Interestingly, the streamwise length-scale of the capillary ridge changes in a way that is directly evaluated using scaling arguments and the predicted power law of $De^{1/4}$ compares favorably with our numerical computations. Regarding the effect of inertia forces, it is found that as Re increases up to moderate values, both capillary waves, near the step-down and step-up, become narrower but further rise leads to a series of damped capillary waves which act more globally as compared to the effect of capillarity. It appears, though, that the dependence of the streamwise length-scale of these features on the material elasticity is not significant, in accordance with the predictions of an order-of-magnitude analysis. At the highest value of Re that we have examined, the surface topology changes drastically, i.e. the capillary waves disappear from the region near the step down while an inertial ridge arises immediately after the step up; these features arise also for a

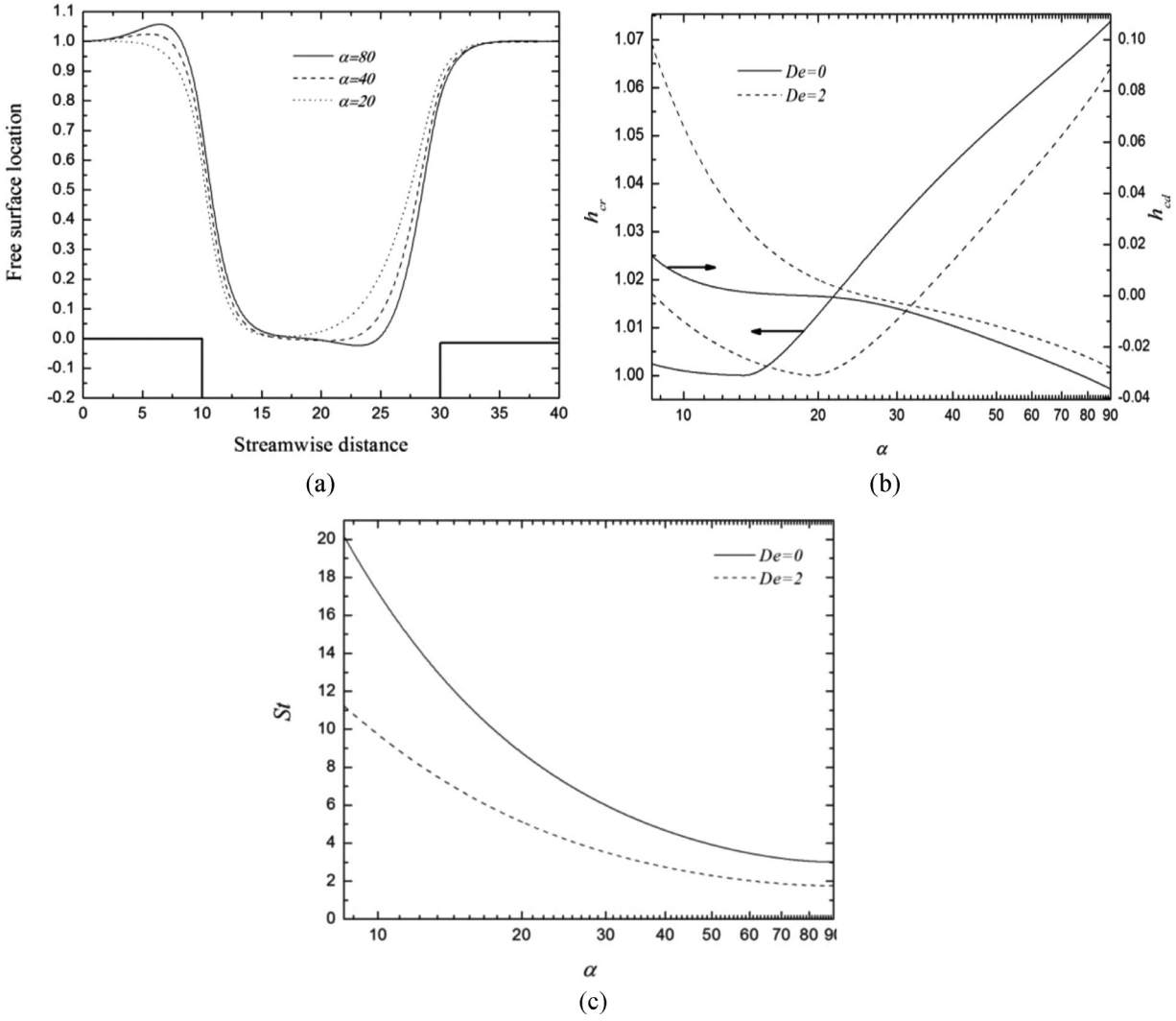

Fig. 13. Dependence of (a) shapes of the predicted free surfaces, (b) deviation height relative to Newtonian free surface, $h_v - h_n$, on inclination angle, α for $De = 2$. (d) Dependence of St on a for $De = (0,\ 2)$. The remaining parameters are $Re = 0$, $Ca = 0.1$, $\varepsilon = 0.05$, $\beta = 0.1$, $l_1 = l_3 = 10$, $l_2 = 20$ and $d = -1$.

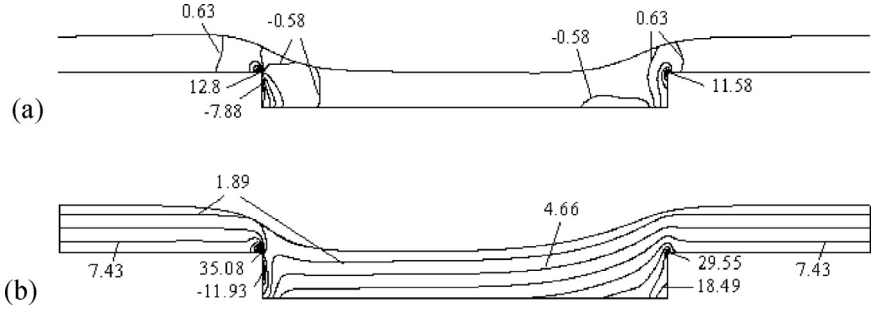

Fig. 14. Pressure contours for (a) $\alpha = 90^\circ$ and (b) $\alpha = 20^\circ$. The remaining parameters are $Re = 0$, $Ca = 0.1$, $De = 2$, $\varepsilon = 0.05$, $\beta = 0.1$, $l_1 = l_3 = 10$, $l_2 = 20$ and $d = -1$.

Newtonian fluid but seem to intensify with increasing material elasticity. We also investigate the effect of geometrical characteristics of the substrate as well as its inclination angle with respect to the acceleration of gravity. Interface deformation is more prominent as the trench becomes broader or deeper. In the case of narrow cavities strong recirculation takes place inside the cavity and as a result the bulk liquid prefers not to enter in the trench but to flow over it. Finally, regarding the effect of the inclination angle it is shown that as the film becomes more horizontal the effect of capillarity diminishes (increases) near the step-up (step-down) due to the increased effect of gravity in the transverse direction of the flow.

The present analysis is based on the usual assumption that the film will wet the cavity completely. This may not be the case in general, as we have demonstrated for Newtonian liquids recently, Lampropoulos et al. [41]. Moreover, our study leaves open the question about the stability of the computed steady solutions. Newtonian films flowing over the limited length of the topography have been shown to be remarkably stable as opposed to the development of travelling and solitary waves that arise in film flows

over a planar wall (Kalliadasis & Homsy [18]). On the other hand, the effect of elasticity in the absence of topography has been examined in detail by Shaqfeh et al. [31]. These authors have shown that the effect of elasticity can be quite involved even in the case of a flat substrate. For small Reynolds numbers and *De* of O(1) viscoelasticity destabilizes the flow, exhibiting though very small growth rates, whilst for large values of *De* it was shown that the elastic effects actually have a stabilizing effect on the flow. The presence of topography will certainly complicate things even further. Hence, this study must be supplemented not only by examining the stability of the present solutions, taking into account the effect of streamwise and spanwise disturbances, but also by allowing the film to partially wet the entire surface of the cavity in the substrate. Such efforts are under way.

Acknowledgements

This work has been supported financially by the General Secretariat of Research and Technology of Greece through the program "Excellence" (Grant No. 1918, entitled "FilCoMicrA") in the framework "Education and Lifelong Learning" co-funded by the European Social Fund and National Resources and the LIMMAT foundation under the grant MuSiComPS.

References

[1] L.E. Stillwagon, R.G. Larson, Levelling of thin film flows over uneven substrates during spin coating, Phys. Fluids A 2 (11) (1990) 1937–1944.
[2] G.L. Booth, Coating Equipment and Processes, Lockwood, New York, 1970.
[3] X. Yin, S. Kumar, Flow visualization of the liquid-emptying process in scaled-up gravure grooves and cells, Chem. Eng. Sci. 61 (2006) 1146–1156.
[4] L.W. Schwartz, P. Moussalli, P. Campbell, R.R. Eley, Numerical modeling of liquid withdrawal from gravure cavities in coating operations, Trans. IChemE 76 (1998) 22–28.
[5] K. Argyriadi, M. Vlachogiannis, V. Bontozoglou, Experimental study of inclined film flow along periodic corrugations: The effect of wall steepness, Phys. Fluids 18 (2006) 012102.
[6] N.J. Balmforth, R.V. Craster, A.C. Rust, R. Sassi, Viscoplastic flow over an inclined surface, J. Non-Newt. Fluid Mech. 142 (2007) 219–243.
[7] M. Pavlidis, Y. Dimakopoulos, J. Tsamopoulos, Steady viscoelastic film flow over 2D topography: I. The effect of viscoelastic properties under creeping flow, J. Non-Newt. Fluid Mech. 165 (2010) 576–591.
[8] Z. Cao, M. Vlachogiannis, V. Bontozoglou, Experimental evidence for a short-wave global mode in film flow along periodic corrugations, J. Fluid Mech. 718 (2013) 304–320.
[9] M.M.J. Decré, J.C. Baret, Gravity-driven flows of low-viscosity liquids over topographies, J. Fluid Mech. 487 (2003) 147–166.
[10] A. Wierschem, N. Aksel, Influence of inertia on eddies created in films creeping over strongly undulated substrates, Phys. Fluids 16 (2004) 4566–4574.
[11] M. Scholle, A. Haas, N. Aksel, M.C.T. Wilson, H.M. Thompson, P.H. Gaskell, Competing geometric and inertial effects on local flow structure in thick gravity–driven fluid films, Phys. Fluids 20 (2008) 123101.
[12] C. Pozrikidis, The flow of a liquid film along a periodic wall, J. Fluid Mech. 188 (1988) 275–300.
[13] A. Mazouchi, G.M. Homsy, Free surface Stokes flow over topography, Phys. Fluids 13 (10) (2001) 2751–2761.
[14] M.G. Blyth, C. Pozrikidis, Film flow down an inclined plane over a three-dimensional obstacle, Phys. Fluids 18 (2006) 052104.
[15] S. Kalliadasis, C. Bielarz, G.M. Homsy, Steady free-surface thin film flows over topography, Phys. Fluids 12 (8) (2000) 1889–1898.
[16] D. Tseluiko, M.G. Blyth, D.T. Papageorgiou, J.M. Vanden-Broeck, Electrified viscous thin film flow over topography, J. Fluid Mech. 597 (2008) 449–475.
[17] R.D. Lenz, S. Kumar, Steady two-layer flow in a topographically patterned channel, Phys. Fluids 19 (2007) 102103.
[18] S. Kalliadasis, G.M. Homsy, Stability of free-surface thin-film flows over topography, J. Fluid Mech. 448 (2001) 387–410.
[19] C. Bielarz, S. Kalliadasis, Time-dependent free-surface thin film flows over topography, Phys. Fluids 15 (2003) 2512–2524.
[20] N. Fraysse, G.M. Homsy, An experimental study of rivulet instabilities in centrifugal spin coating of viscous Newtonian and non-Newtonian fluids, Phys. Fluids 6 (4) (1994) 1491–1504.
[21] P.H. Gaskell, P.K. Jimack, M. Sellier, H.M. Thompson, C.T. Wilson, Gravity-driven flow of continuous thin liquid films on non-porous substrates with topography, J. Fluid Mech. 509 (2004) 253–280.
[22] S. Veremieiev, H.M. Thompson, Y. Lee, P.H. Gaskell, Inertial thin film flow on planar surfaces featuring topography, Comp. Fluids 39 (2010) 431–450.
[23] C. Zhou, S. Kumar, Two-dimensional two-layer channel flow near a step, Chem. Eng. Sci. 81 (2012) 38–45.
[24] C. Heining, V. Bontozoglou, N. Aksel, A. Wierschem, Nonlinear resonance in viscous films on inclined wavy walls, Inter. J. Multiph. Flow 35 (2009) 78–90.
[25] N. Malamataris, V. Bontozoglou, Computer aided analysis of visous film flow along an inclined wavy wall, J. Comp. Phys. 154 (1999) 372–392.
[26] V. Bontozoglou, K. Serifi, Falling film flow along steep two-dimensional topography: The effect of inertia, J. Multiph. Flow 34 (8) (2008) 734–747.
[27] S. Saprykin, R.J. Koopmans, S. Kalliadasis, Free-surface thin-film flows over topography: influence of inertia and viscoelasticity, J. Fluid Mech. 578 (2007) 271–293.
[28] N. Phan-Tien, H.T. Low, Squeeze-film flow of a viscoelastic fluid a lubrication model, J. Non Newt. Fluid Mech. 28 (1988) 129–148.
[29] N. Phan-Tien, J. Dudek, D.V. Boger, V. Tirtaatmadja, Squeeze film flow of ideal elastic liquids, J. Non Newt. Fluid Mech. 18 (1985) 227–254.
[30] G. Karapetsas, V. Bontozoglou, Non-linear dynamics of a viscoelastic film subjected to a spatially periodic electric field, J. Non Newt. Fluid Mech. 217 (2015) 1–13.
[31] E.S.G. Shaqfeh, R.G. Larson, G.H. Fredrickson, The stability of gravity driven viscoelastic film-flow at low to moderate Reynolds number, J. Non Newt. Fluid Mech. 31 (1989) 87–113.
[32] N. Phan-Thien, R.I. Tanner, A new constitutive equation derived from network theory, J. Non-Newtonian Fluid Mech. 2 (1977) 353–365.
[33] N. Phan-Thien, A nonlinear network viscoelastic model, J. Rheol. 22 (1978) 259–283.
[34] D. Rajagopalan, R.C. Armstrong, R.A. Brown, Finite element methods for calculation of steady, viscoelastic flow using constitutive equations with Newtonian viscosity, J. Non-Newt. Fluid Mech. 36 (1990) 159–192.
[35] R.A. Brown, M.J. Szady, P.J. Northey, R.C. Armstrong, On the numerical stability of mixed finite-element methods for viscoelastic flows governed by differential constitutive equations, Theor. Comp. Fluid Dyn. 5 (1993) 77–106.
[36] Y. Dimakopoulos, J. Tsamopoulos, A quasi-elliptic transformation for moving boundary problems with large anisotropic deformations, J. Comp. Phys. 192 (2003) 494–522.
[37] N. Chatzidai, A. Giannousakis, Y. Dimakopoulos, J. Tsamopoulos, On the elliptic mesh generation in domains containing multiple inclusions and undergoing large deformations, J. Comp. Phys. 228 (2009) 1980–2011.
[38] D.J. Benney, Long waves on liquid films, J. Math. Phys. 45 (1966) 150–155.
[39] W.B. Krantz, S.L. Goren, Finite-amplitude, long waves on liquid films flowing down a plane, Ind. Eng. Chem. Res. Fundam. 9 (1970) 107–113.
[40] R.W. Atherton, G.M. Homsy, On the derivation of evolution equations for interfacial waves, Chem. Eng. Comm. 2 (1976) 55–77.
[41] N. Lampropoulos, Y. Dimakopoulos, J. Tsamopoulos, Transient flow of gravity–driven viscous films over substrates with rectangular topographical features, Microfluid Nanofluid 20 (2016) 51.